



## NRC Publications Archive Archives des publications du CNRC

### **Structural and optical properties of axial silicon-germanium nanowire heterojunctions**

Wang, X.; Tsybeskov, L.; Kamins, T. I.; Wu, X.; Lockwood, D. J.

This publication could be one of several versions: author's original, accepted manuscript or the publisher's version. / La version de cette publication peut être l'une des suivantes : la version prépublication de l'auteur, la version acceptée du manuscrit ou la version de l'éditeur.

For the publisher's version, please access the DOI link below. / Pour consulter la version de l'éditeur, utilisez le lien DOI ci-dessous.

#### **Publisher's version / Version de l'éditeur:**

<https://doi.org/10.1063/1.4937345>

*Journal of Applied Physics*, 118, pp. 23430-1-234301-8, 2015

#### **NRC Publications Record / Notice d'Archives des publications de CNRC:**

<https://nrc-publications.canada.ca/eng/view/object/?id=8283ffbf-e8c6-4048-97e6-15b22e5c8bc9>

<https://publications-cnrc.canada.ca/fra/voir/objet/?id=8283ffbf-e8c6-4048-97e6-15b22e5c8bc9>

Access and use of this website and the material on it are subject to the Terms and Conditions set forth at

<https://nrc-publications.canada.ca/eng/copyright>

READ THESE TERMS AND CONDITIONS CAREFULLY BEFORE USING THIS WEBSITE.

L'accès à ce site Web et l'utilisation de son contenu sont assujettis aux conditions présentées dans le site

<https://publications-cnrc.canada.ca/fra/droits>

LISEZ CES CONDITIONS ATTENTIVEMENT AVANT D'UTILISER CE SITE WEB.

#### **Questions?** Contact the NRC Publications Archive team at

PublicationsArchive-ArchivesPublications@nrc-cnrc.gc.ca. If you wish to email the authors directly, please see the first page of the publication for their contact information.

**Vous avez des questions?** Nous pouvons vous aider. Pour communiquer directement avec un auteur, consultez la première page de la revue dans laquelle son article a été publié afin de trouver ses coordonnées. Si vous n'arrivez pas à les repérer, communiquez avec nous à PublicationsArchive-ArchivesPublications@nrc-cnrc.gc.ca.



## Structural and optical properties of axial silicon-germanium nanowire heterojunctions

X. Wang, L. Tsybeskov, T. I. Kamins, X. Wu, and D. J. Lockwood

Citation: *Journal of Applied Physics* **118**, 234301 (2015); doi: 10.1063/1.4937345

View online: <http://dx.doi.org/10.1063/1.4937345>

View Table of Contents: <http://scitation.aip.org/content/aip/journal/jap/118/23?ver=pdfcov>

Published by the [AIP Publishing](#)

---

### Articles you may be interested in

[Structural and optical characterization of GaN nanowires](#)

*J. Appl. Phys.* **113**, 204303 (2013); 10.1063/1.4808097

[Optical properties of “black silicon” formed by catalytic etching of Au/Si\(100\) wafers](#)

*J. Appl. Phys.* **113**, 173502 (2013); 10.1063/1.4803152

[Influence of catalytic gold and silver metal nanoparticles on structural, optical, and vibrational properties of silicon nanowires synthesized by metal-assisted chemical etching](#)

*J. Appl. Phys.* **112**, 073509 (2012); 10.1063/1.4757009

[Structural and optical properties of InGaN–GaN nanowire heterostructures grown by molecular beam epitaxy](#)

*J. Appl. Phys.* **109**, 014309 (2011); 10.1063/1.3530634

[Structural and optical properties of Zn<sub>0.9</sub>Mn<sub>0.1</sub>O / ZnO core-shell nanowires designed by pulsed laser deposition](#)

*J. Appl. Phys.* **106**, 093501 (2009); 10.1063/1.3253572

---

A promotional banner for AIP Applied Physics Reviews. The background is a dark blue gradient with a bright light source on the right, creating a lens flare effect. On the left, there is a small image of a journal cover titled 'AIP Applied Physics Reviews' featuring a diagram of a nanowire structure. The main text 'NEW Special Topic Sections' is in large, white, bold font. Below this, the text 'NOW ONLINE' is in yellow, followed by 'Lithium Niobate Properties and Applications: Reviews of Emerging Trends' in white. The AIP Applied Physics Reviews logo is in the bottom right corner.

**NEW Special Topic Sections**

**NOW ONLINE**  
Lithium Niobate Properties and Applications:  
Reviews of Emerging Trends

**AIP** Applied Physics  
Reviews

# Structural and optical properties of axial silicon-germanium nanowire heterojunctions

X. Wang,<sup>1</sup> L. Tsybeskov,<sup>1,a)</sup> T. I. Kamins,<sup>2</sup> X. Wu,<sup>3</sup> and D. J. Lockwood<sup>3</sup>

<sup>1</sup>*ECE Department, New Jersey Institute of Technology, Newark, New Jersey 07102, USA*

<sup>2</sup>*Department of Electrical Engineering, Stanford University, Stanford, California 94305, USA*

<sup>3</sup>*National Research Council, Ottawa, Ontario K1A 0R6, Canada*

(Received 14 September 2015; accepted 24 November 2015; published online 15 December 2015)

Detailed studies of the structural and optical properties of axial silicon-germanium nanowire heterojunctions show that despite the 4.2% lattice mismatch between Si and Ge they can be grown without a significant density of structural defects. The lattice mismatch induced strain is partially relieved due to spontaneous SiGe intermixing at the heterointerface during growth and lateral expansion of the Ge segment of the nanowire. The mismatch in Ge and Si coefficients of thermal expansion and low thermal conductivity of Si/Ge nanowire heterojunctions are proposed to be responsible for the thermally induced stress detected under intense laser radiation in photoluminescence and Raman scattering measurements. © 2015 AIP Publishing LLC.

[<http://dx.doi.org/10.1063/1.4937345>]

## I. INTRODUCTION

Germanium is a group IV semiconductor with a room temperature direct bandgap of 0.8 eV ( $\sim 1.55 \mu\text{m}$ ), and it is separated by only 0.14 eV from the indirect band gap of 0.66 eV. These properties make Ge one of the most promising materials for CMOS compatible photonic components including near-infra-red photodetectors<sup>1–4</sup> and, possibly, lasers<sup>5–7</sup> in the important spectral region of 1.3–1.6  $\mu\text{m}$ . However, it is well known that conventional Ge heteroepitaxy on Si is complicated by the 4.2% difference in Ge and Si lattice constants.<sup>8,9</sup> Various techniques for building quality Si/Ge heterojunctions (HJs) include multi-step annealing to relax Ge layers and reduce the dislocation density,<sup>10,11</sup> growth of ultra-thin Ge films and superlattices using Si<sub>1–x</sub>Ge<sub>x</sub> alloy transition layers with graded Ge composition  $x$ ,<sup>8,11–14</sup> and three-dimensional (3D) growth in the form of SiGe clusters and cluster multi-layers using the Stranski-Krastanov (S-K) growth mode.<sup>15–18</sup> Another promising approach is to use one-dimensional (1D) growth in the form of nanowires (NWs) produced by the vapor-liquid-solid (VLS) growth mode or similar techniques.<sup>19–22</sup> These axial Si/Ge NW HJs with the heterointerfaces perpendicular to the NW axes have a reduced heterointerface area compared to radial or “core-shell” NW HJs, where the Si/Ge heterointerfaces are parallel to the NW axes.<sup>22–24</sup> Since Ge has a larger lattice constant (5.658 Å) compared to Si (5.431 Å), it was proposed that in axial Si/Ge NW HJs strain created by the lattice mismatch between Si and Ge can partially be relieved at the heterointerfaces by the lateral expansion of a Ge segment of the NW.<sup>25,26</sup> Thus, the fabrication and study of Si/Ge NW HJs might open interesting opportunities in building low defect density nanostructures for applications in CMOS compatible photonic components.

## II. EXPERIMENTAL DETAILS

In this study, axial Si/Ge NW HJs are grown using the VLS technique and Au nanoparticles as a precursor in a reduced pressure, lamp heated chemical vapor deposition (CVD) reactor using the following growth steps:<sup>27</sup>

- (1) A thin layer of Au ( $\sim 2 \text{ nm}$  thick) is deposited on a cleaned, p-type (111) Si substrate with a resistivity of 0.01–0.02  $\Omega \text{ cm}$  and annealed for 10 min at 670 °C at 95 Torr in a H<sub>2</sub> ambient to form nanometer-size clusters. For details, see Ref. 28.
- (2) The Si segments of the NWs are grown at 680 °C at 30 Torr using the gaseous precursors SiH<sub>4</sub> and HCl in a H<sub>2</sub> ambient. The growth rate for the Si NW segment is estimated to be close to 100 nm per minute.<sup>28</sup>
- (3) The reactor is cooled to 350 °C at a nominal rate of 75 °C/min with the SiH<sub>4</sub>-HCl-H<sub>2</sub> mixture flowing.
- (4) The Ge segments of the NWs are grown at 350 °C and 90 Torr, using GeH<sub>4</sub> and HCl as the gaseous precursors in the H<sub>2</sub> ambient. The growth rate for the Ge NW segment is estimated to be 40 nm per minute.<sup>29</sup>
- (5) To avoid sample oxidation, before samples are exposed to air the reactor is cooled down to room temperature. We find that most of the studied Si/Ge NW HJ samples have a NW diameter ranging from 50 to 130 nm. The total NW length is 1500–2000 nm with the Ge segment as long as 500 nm.

Samples are characterized using a JEOL JEM-2100F field emission source transmission electron microscope (TEM) operating at 200 kV equipped with an Oxford INCA energy-dispersive x-ray spectrometer (EDX) with a probe size of 0.2 nm. Raman scattering measurements are performed using a Jobin Yvon U1000 double-grating, 1 m focal length monochromator with a thermoelectrically cooled Hamamatsu R943–02 photomultiplier tube (PMT) and a photon counting system. The Raman system spectral resolution

<sup>a)</sup>Electronic mail: [tsybesko@njit.edu](mailto:tsybesko@njit.edu)

is up to  $0.25 \text{ cm}^{-1}$ . In order to analyze polarized Raman scattering, a rotating thin-film polarizer has been used. A continuous-wave (CW) multi-line  $\text{Ar}^+$  laser has been used as an excitation source with the focused laser spot size of  $50 \times 50 \mu\text{m}^2$ . The laser light incident angle is close to Brewster's angle, and the measured reflection is  $\leq 3\%$ . In these experiments, the excitation intensity has been varied from  $10^2$  to  $10^3 \text{ W/cm}^2$ . Photoluminescence (PL) measurements are performed at normal incidence with a light spot of  $50 \times 50 \mu\text{m}^2$  using a single-grating Acton Research 0.5 m focal length monochromator and detected by a Ge photodetector or by a thermoelectrically cooled InGaAs photomultiplier operating in the  $0.9\text{--}1.65 \mu\text{m}$  spectral region.

### III. RESULTS AND DISCUSSION

#### A. TEM and EDX

Figure 1 shows a moderate resolution TEM image of a single axial Si/Ge NW HJ with a clearly visible Si/Ge heterointerface and smooth NW surface. The diameter of the Si segment of the NW is  $\sim 105 \text{ nm}$ , and it is nearly constant. The diameter of the Ge segment of the NW gradually increases from  $\sim 105$  to  $115 \text{ nm}$  within  $\sim 100\text{--}150 \text{ nm}$  from the Si/Ge heterointerface and then remains constant. Figure 2 presents a high resolution TEM image of the Si/Ge NW heterointerface close to the NW center. The lattice fringe spacing confirms the NW (111) crystallographic direction. The inset shows the corresponding lattice fringe spacing fast Fourier transform (FFT) of the marked area (circle) attesting to the nearly ideal crystallinity of the NW center. Figure 3 shows a high-resolution TEM micrograph of the same Si/Ge NW heterojunction with focus on the area close to the NW surface where a  $\sim 1 \text{ nm}$  thick amorphous oxide layer can be seen (marked by an arrow) and structural imperfections are confirmed by the FFT analysis (see area marked by circle and inset). Note that no dislocations are observed in the vicinity of the Si/Ge NW HJ.

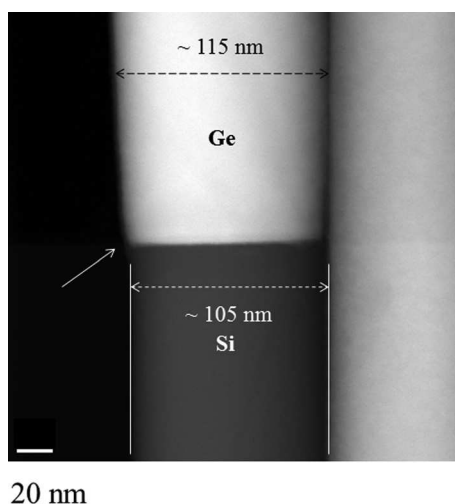


FIG. 1. Transmission electron microscope (TEM) image of the axial Si/Ge nanowire (NW) heterojunction (HJ) showing an abrupt Si/Ge heterointerface and an increase in the NW diameter from  $105 \text{ nm}$  in the Si segment to  $115 \text{ nm}$  in the Ge segment of the NW.

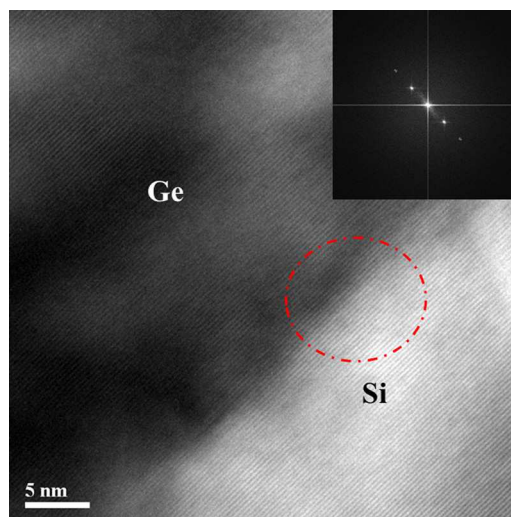


FIG. 2. High-resolution TEM image of the Si/Ge NW HJ interface close to the NW center with clearly evident (111) lattice fringes. A fast Fourier transform (FFT) of the circle marked area is shown in the inset.

Results of compositional EDX microanalysis of the Si/Ge NW HJs are shown in Fig. 4. Similar results were obtained from other EDX scans across the heterointerface near the center and close to the edge of the NW. The Si/Ge NW HJ is comprised of Si and Ge NW segments with a clearly observed  $\sim 8 \text{ nm}$  thick SiGe transition layer produced by spontaneous SiGe intermixing during growth. The EDX data indicate that a  $2 \text{ nm}$  thick  $\text{Si}_{0.8}\text{Ge}_{0.2}$  layer is formed close to the Si segment of the NW, and this is known to be a stable SiGe alloy composition produced by spontaneous intermixing.<sup>30,31</sup> This is an interesting observation, because the Ge segment of the NW is deposited using a relatively low ( $350^\circ\text{C}$ ) deposition temperature. Most likely, this SiGe transition layer is a result of the presence of residual Si atoms in the eutectic Si-Au alloy after switching to Ge deposition and strain-driven interdiffusion.

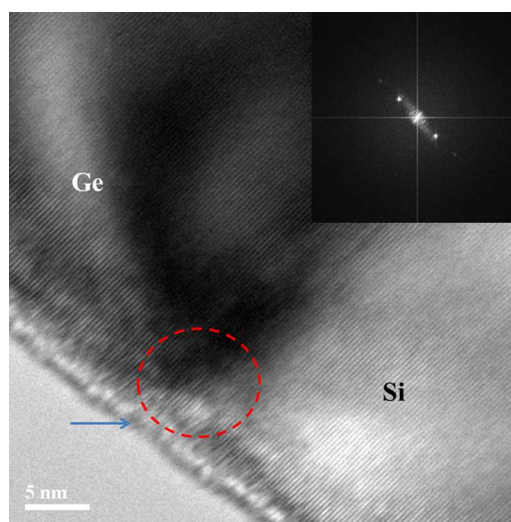


FIG. 3. High-resolution TEM image of the Si/Ge NW HJ interface close to the NW surface with clearly observed distortion of the lattice fringes and the corresponding FFT of the circle marked area (inset). An amorphous layer of  $\sim 1 \text{ nm}$  thickness at the NW surface is indicated by an arrow.

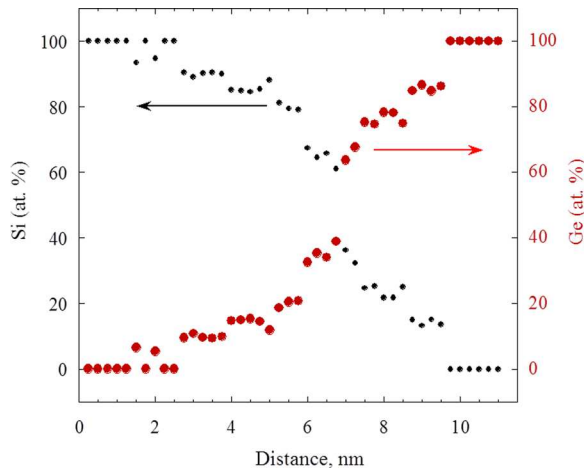


FIG. 4. Compositional analysis of the NW along the growth direction, showing a spontaneously formed SiGe alloy transition layer at the Si-Ge interface.

### B. Photoluminescence

Figure 5(a) compares the normalized Si/Ge NW PL spectra to the c-Si PL spectrum measured at the same ( $T=20$  K) temperature. The Si/Ge NW PL spectra clearly exhibit at least two peaks. A narrower PL peak at  $\sim 1.08$  eV (PL1) and a broader PL peak at  $\sim 1.03$  eV (PL2) are clearly observed, and only a very weak PL signal with photon energies close to the bulk c-Si transverse optical (TO) PL peak at 1.1–1.15 eV is found at  $T=20$  K (marked by an arrow in the figure). Note that no PL associated with c-Ge at 0.7–0.65 eV has been detected. The relative intensities and spectral positions of the two major PL peaks are found to be temperature dependent (Fig. 5(b)): both PL peaks change their positions significantly with temperature. The PL1 peak is detectable even at room temperature and exhibits an asymmetric broadening, which (in agreement with Ref. 32) can be fitted using Boltzmann thermal broadening on the high photon energy

side of the PL spectrum (not shown). The PL peak position temperature dependence is unusual and will be discussed later. Note that a reliable detection of the PL signal at room temperature requires an excitation intensity of  $\sim 600$  W/cm<sup>2</sup>.

### C. Raman scattering

Figure 6(a) shows Raman spectra of Si/Ge NW HJs measured using argon laser excitation at different wavelengths. Under 514.5 nm excitation, we observe three distinct Raman peaks associated with Si-Si ( $\sim 520$  cm<sup>-1</sup>), Si-Ge ( $\sim 400$  cm<sup>-1</sup>), and Ge-Ge ( $\sim 300$  cm<sup>-1</sup>) vibrations with the main Raman peak at 300 cm<sup>-1</sup>. Using 458 nm excitation, we find the same peaks but with the main Raman peak at  $\sim 520$  cm<sup>-1</sup>. This difference is due to a strong spectral dependence of the Raman scattering cross-section and well-known Raman resonances in Ge at 2.2–2.5 eV associated with  $E_1$  and  $E_1 + \Delta_1$  optical transition.<sup>33</sup> Note that a peak at  $\sim 280$  cm<sup>-1</sup> is, most likely, an argon plasma line. A Raman peak at  $\sim 500$  cm<sup>-1</sup> is best observed using 458 nm excitation and is associated with the Si-Si vibration in the presence of a neighboring Ge atom or Si-Si(Ge).<sup>34</sup> The Raman spectra are also sensitive to the excitation intensity. Figure 6(b) shows Raman spectra recorded using three different excitation intensities. As the excitation intensity increases, the major Raman peak at  $\sim 520$  cm<sup>-1</sup> broadens and shifts toward lower wavenumbers (similar behavior is observed for the Raman peaks at 400 and 300 cm<sup>-1</sup>, not shown). However, with increasing excitation intensity, the Raman peak at 500 cm<sup>-1</sup> shifts in the opposite direction. The results of fitting including the Raman peak spectral position, full width at half maximum (FWHM), and ratio of integrated intensities for Raman peaks at 520 and 500 cm<sup>-1</sup> as a function of excitation intensity are shown in Fig. 7. Note that at 458 nm excitation, 10<sup>2</sup> W/cm<sup>2</sup> is the minimum excitation intensity allowing the recording of quality Raman spectra (where reasonable fitting is possible) and the application of more than 10<sup>3</sup> W/cm<sup>2</sup>

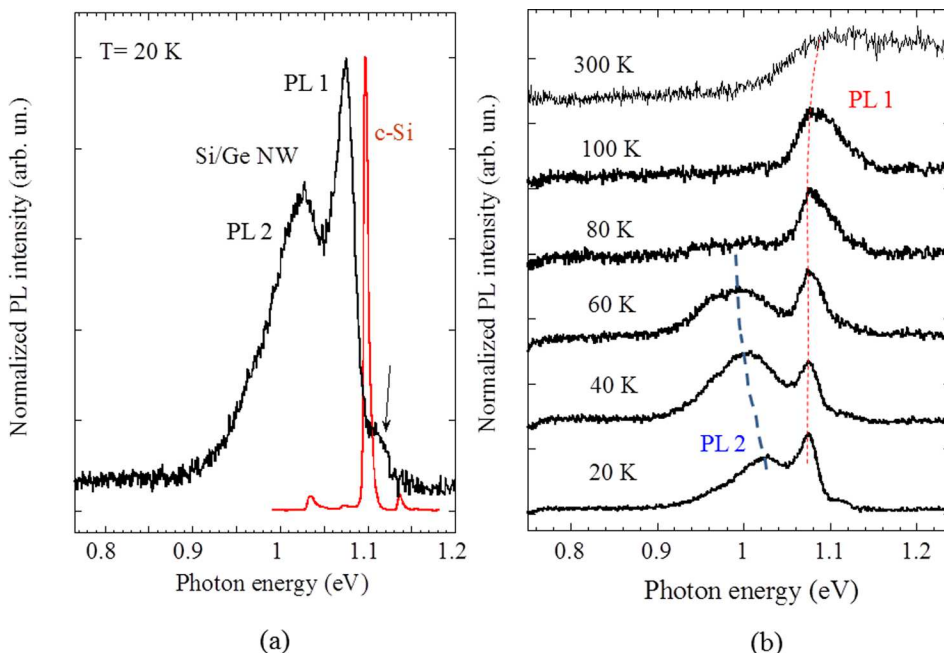


FIG. 5. (a) Comparison of photoluminescence (PL) spectra of the Si/Ge NW HJs and c-Si. (b) The PL spectra of the Si/Ge NW HJs at various (marked) temperatures. The major PL peak shifts with temperature increase are indicated by the dashed lines.

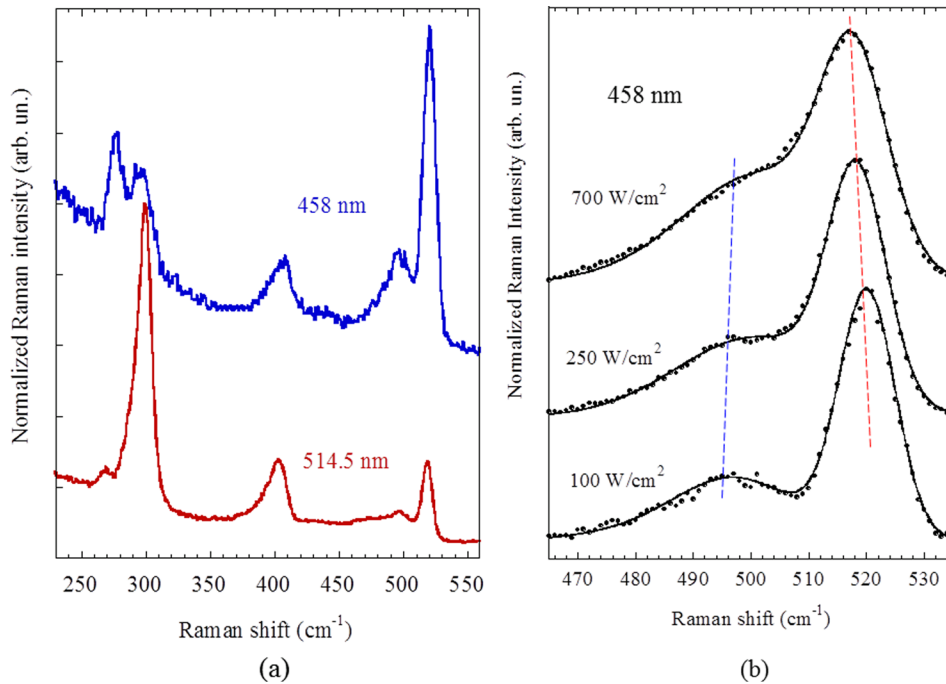


FIG. 6. (a) Raman spectra of Si/Ge NW HJs obtained under different (indicated) excitation wavelengths. (b) Background-corrected Raman spectra obtained under 458 nm wavelength excitation and different (indicated) excitation intensities.

produces irreversible changes in the spectrum, most likely due to laser damage of the studied samples.

Figure 8 shows the intensity of Raman scattering at  $\sim 500 \text{ cm}^{-1}$  as a function of the polarization angle and compares the data with similar measurements using (111)-oriented c-Si. It is clearly observed that at the lowest excitation intensity, the Raman signal polarization dependence is the same as for (111) c-Si and Si/Ge NW HJs, which is due to their (111) crystallographic orientation. However, at higher excitation intensity, the Raman scattering polarization dependence in Si/Ge NW HJs becomes considerably weaker.

#### D. Discussion

The VLS growth mode of Si NWs and Si/Ge NW-based HJs has been intensively investigated.<sup>35–38</sup> It was shown that

in lattice-mismatched NW HJs, structural relaxation can be associated with defects in the form of twin boundaries parallel to the growth axis and directly related to the NW kinking.<sup>35</sup> Also, a rough NW surface typically indicates a high density of surface defects,<sup>39</sup> and in many cases the NW diameter continuously decreases producing so-called “tapered” NWs.<sup>40</sup> It was demonstrated that introducing chlorine-containing species in the gas phase (e.g.,  $\text{SiH}_4\text{-HCl-H}_2$  and  $\text{GeH}_4$  mixed with HCl) greatly inhibits the uncatalyzed material deposition rate, thus yielding NWs with a smooth surface and uniform diameter along their entire length.<sup>41</sup> These results explain why in our samples the majority of NWs have smooth surfaces and nearly constant diameters (except for the lateral expansion of the Ge segment of the NW HJ).

High-resolution TEM studies, analyses of lattice fringes, and EDX measurements (Figs. 1–4) indicate that close to the

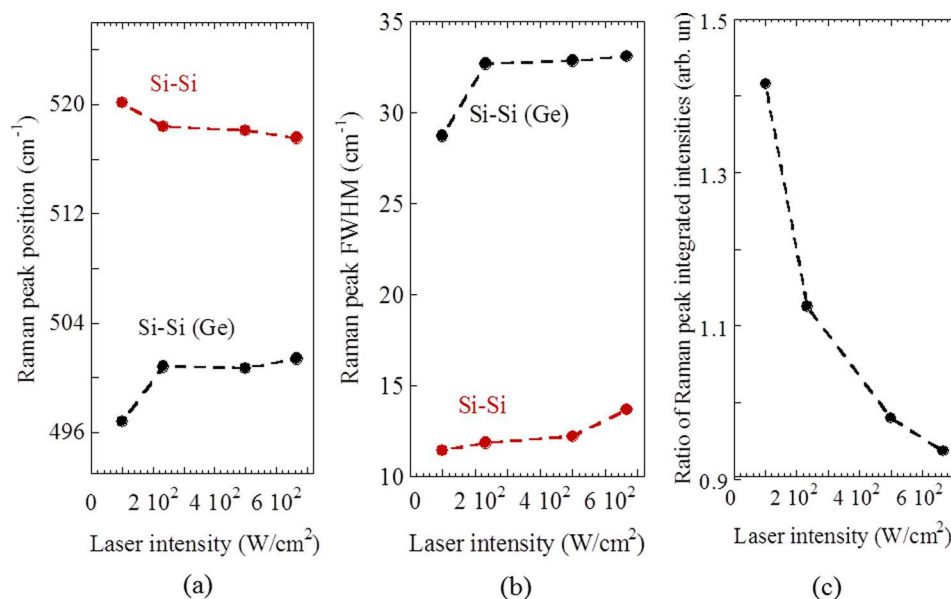


FIG. 7. Comparison of the Raman signals associated with Si-Si and Si-Si(Ge) vibrations in Si/Ge NW HJs: (a) Raman peak position, (b) Raman peak full width at half maximum (FWHM), and (c) ratio of Si-Si to Si-Si(Ge) Raman peak integrated intensities as a function of the 458 nm excitation intensity.

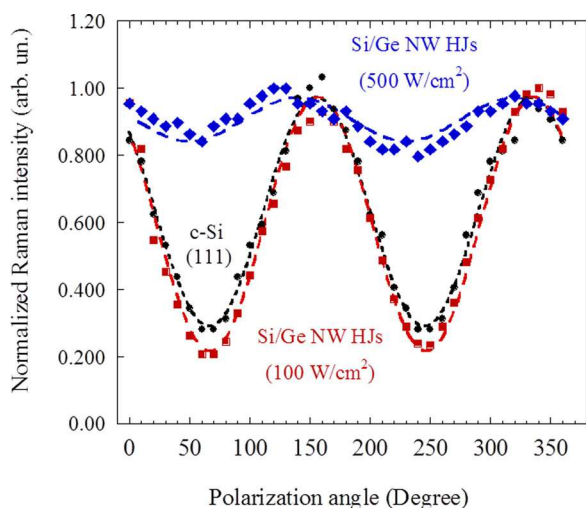


FIG. 8. Raman signal polarization dependence in (111) c-Si and Si/Ge NW HJs under different (indicated) excitation intensities. The dashed lines are fits to the experimental points.

center of the NW in the vicinity of the Si/Ge HJ the lattice-mismatch induced strain is partially relaxed via spontaneous intermixing and the formation of an  $\sim 8$  nm thick SiGe transition layer. Additional structural relaxation occurs by gradual (within  $\sim 100$  nm from the Si/Ge heterointerface) lateral expansion (i.e., increase in diameter) of the Ge segment of the NW (Fig. 1). Close to the NW surface, we find a distortion in the lattice fringe patterns, which is easily detected by TEM-based FFT analysis (Fig. 3 inset). These structural imperfections are located within a 2–3 nm thick interface layer between the NW core and an oxide layer at the NW surface, and they are slightly extended (up to 5–6 nm) toward the NW core in the vicinity of the Si/Ge NW HJs (Fig. 3). We find that the Si/Ge NW HJs with a diameter approaching 70–100 nm can have a nearly perfect crystalline core and overall smaller density of structural defects (due to a smaller surface-to-volume ratio) compared to thinner NWs.

Examination of the spacing between the lattice fringes in different regions of the central portion of the NW (Fig. 2) shows that 15–20 nm away from the Si/Ge heterointerface the lattice constants are similar to those of the respective bulk materials. Starting at the Si-Ge interface, the lattice constant increases from that of Si to that of Ge in parallel with the increase in the Ge concentration, and thus the lattice-mismatch strain expected between Si and Ge is largely relieved during growth by the smooth alloy composition variation in the 8 nm thick transition region (Fig. 4).

We do not find any significant PL at energies close to the c-Ge energy gap, most likely due to the following reasons. Both of the Si and Ge segments of the HJs exhibit high crystallinity (Fig. 2) and, therefore, should have reasonably long carrier diffusion lengths, similar to that in bulk Si and Ge. Also, both segments are covered by a thin amorphous oxide layer with visible imperfections near the NW surface (Fig. 3). Since Si and Ge are both indirect band gap semiconductors with a long carrier radiative lifetime, excitons/electron-hole pairs have enough time to diffuse toward the surface and recombine at surface defect states, mostly non-radiatively. The  $\text{GeO}_2/\text{Ge}$  interface is more defective compared to the

$\text{SiO}_2/\text{Si}$  interface, and thus no PL associated with the pure Ge segment of the NW is observed.<sup>29</sup>

In the Si segment of the NW, our TEM studies detect a 15–20 nm long strained Si region close to the Si/Ge NW hetero-interface. The PL1 peak at 1.08 eV, most likely, is associated with this strained Si region where the energy gap is slightly narrower compared to that in c-Si.<sup>42</sup> The narrower energy gap Si region of the NW collects excitons (and/or electron-hole pairs) quite effectively. This process is even more efficient at the Si/Ge hetero-interface, where the  $\sim 8$  nm thick SiGe alloy layer is found. In SiGe alloys and nanostructures, compositional fluctuation is known to be responsible for low-temperature exciton localization,<sup>43</sup> therefore, exciton diffusion toward the surface is suppressed. Also, SiGe compositional fluctuation is responsible for the reduction of the exciton radiative lifetime.<sup>44</sup> Thus, the low-temperature PL peak at 1.03 eV (PL2) is attributed to radiative recombination of excitons localized at the  $\sim 8$  nm thick SiGe NW hetero-interface.<sup>27</sup> This conclusion is supported by the PL2 peak temperature dependence: the PL2 peak disappears at  $T > 80$  K, and this is consistent with a less than 10 meV SiGe composition-fluctuation-related exciton localization energy.<sup>30,31</sup>

Considering the PL peak position temperature dependence, the PL peak associated with band-to-band radiative recombination should follow the energy band gap temperature dependence  $E_G(T)$ . In bulk c-Si, the PL peak energy position and line-shape temperature dependencies are explained by taking into account the exciton binding energy ( $E_{\text{exc}} \approx 10$  meV), the phonon-assisted nature of the band-to-band recombination involving mostly TO phonons ( $E_{\text{ph}} \approx 60$  meV) and the temperature dependence of population of energy states in the energy bands.<sup>32</sup> Thus, the band-to-band recombination related PL peak photon energy is  $E_{\text{PL}} = E_G - (E_{\text{ph}} + E_{\text{exc}})$ , and in bulk c-Si at low temperature it is close to 1.1 eV. The temperature dependencies of  $E_G(T)$  and  $E_{\text{PL}}(T)$  in c-Si are shown in Fig. 9(a).

In Si/Ge NW HJs, the two major PL peaks exhibit a very different dependence on temperature. As the temperature increases, the PL1 peak shows an almost continuous shift toward higher photon energies (Fig. 9(a)), and above 170 K it crosses the expected bulk c-Si PL peak position. Assuming that this PL is associated with band-to-band recombination within the Si NW segment, this behavior indicates the presence of significant thermal stress. Note that at elevated temperatures ( $T > 250$  K), the PL intensity decreases significantly. Thus, the PL measurements require a high ( $\geq 600$   $\text{W}/\text{cm}^2$ ) excitation intensity, and laser induced NW heating takes place, which is discussed below). Also, at elevated temperatures, a broad and weak PL peak appears at 1.2–1.25 eV, which is most likely associated with NW surface defects, and it becomes comparable in intensity with the PL1 peak (see the PL spectrum at 300 K in Fig. 5(b)).

We find that the PL2 peak (presumably associated with the NW Si/Ge interface region) follows the direction of the Si coefficient of thermal expansion (CTE) temperature dependence. As temperature increases from 20 to 60 K, the Si CTE first decreases and then increases with a minimum around 70 K,<sup>45</sup> while the Ge CTE monotonically increases

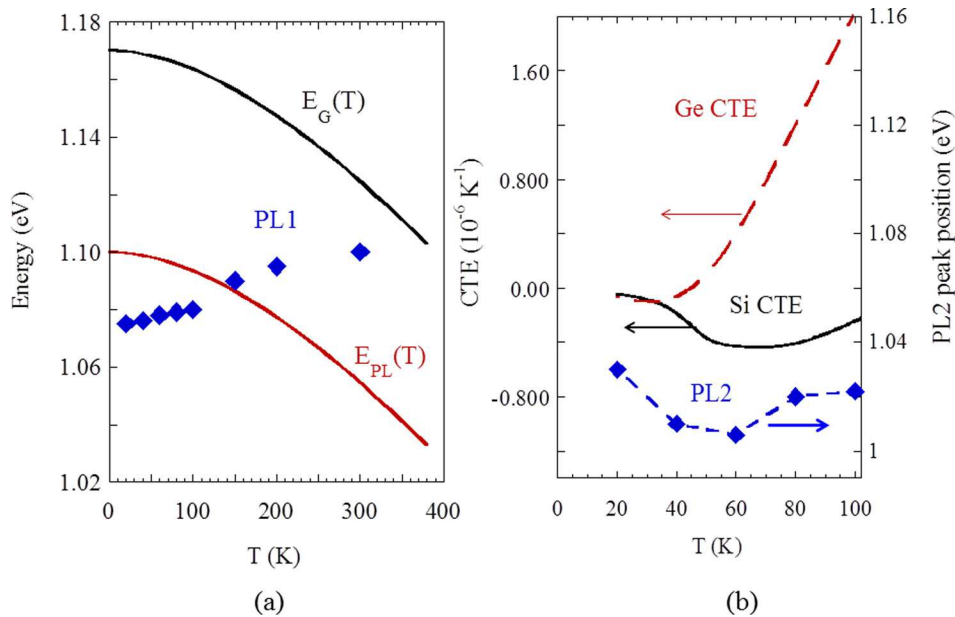


FIG. 9. (a) Temperature dependencies of c-Si energy gap, c-Si PL peak position, and PL1 peak position in Si/Ge NW HJs. (b) Comparison of the temperature dependencies of the coefficient of thermal expansion (CTE) in c-Si and c-Ge and the PL2 peak position in Si/Ge NW HJs. Note that the experimentally measured temperature is the sample holder temperature.

(Fig. 9(b)). We believe that the PL2 peak position is affected by temperature dependent strain in Si/Ge NW HJs due to the large difference in the Si and Ge CTE temperature dependencies.<sup>27</sup>

On considering the Raman measurements, we anticipate that under the applied laser excitation intensity of  $10^2$ – $10^3 \text{ W/cm}^2$  the sample temperature increases, and such temperature increase can be detected by monitoring the Raman peak wavenumber and FWHM temperature dependencies.<sup>46,47</sup> Generally, as temperature increases, the Raman peak shifts toward lower wavenumber due to thermal expansion and changes in the self-energy of the vibrational mode.<sup>46</sup> At the same time, the Raman peak FWHM increases, mainly due to energy relaxation processes (i.e., the decay of the Raman phonon into various optical/acoustical phonons, etc.).<sup>47</sup> Thus, by knowing the initial (room temperature) Raman peak wavenumber/FWHM and their temperature dependencies,<sup>46,47</sup> one

can accurately calculate the sample temperature by measuring the shift and broadening of the Raman spectra.

Figure 10 compares the Si-Si Raman peak position and FWHM in Si/Ge NW HJs with the theoretically predicted and experimentally confirmed temperature dependencies of that in bulk c-Si.<sup>46,47</sup> The Si-Si Raman peak position in Si/Ge NW HJs is in full agreement with the bulk c-Si Raman temperature dependence calculated by using Ref. 46 (Fig. 10(a)), and under  $700 \text{ W/cm}^2$  excitation the sample temperature is estimated to be  $\sim 410 \text{ K}$ . This significant laser heating of our samples is due to a reduced thermal conductivity of the Si/Ge NW HJs compared to that in c-Si.<sup>48</sup>

The Si-Si Raman peak FWHM temperature dependence in Si/Ge NW HJs follows that in bulk c-Si<sup>47</sup> but with an almost four times greater value (Fig. 10(b)). The initial broadening of the Si-Si Raman peak in Si/Ge NW HJs can be attributed to a non-uniform strain, which is also expected

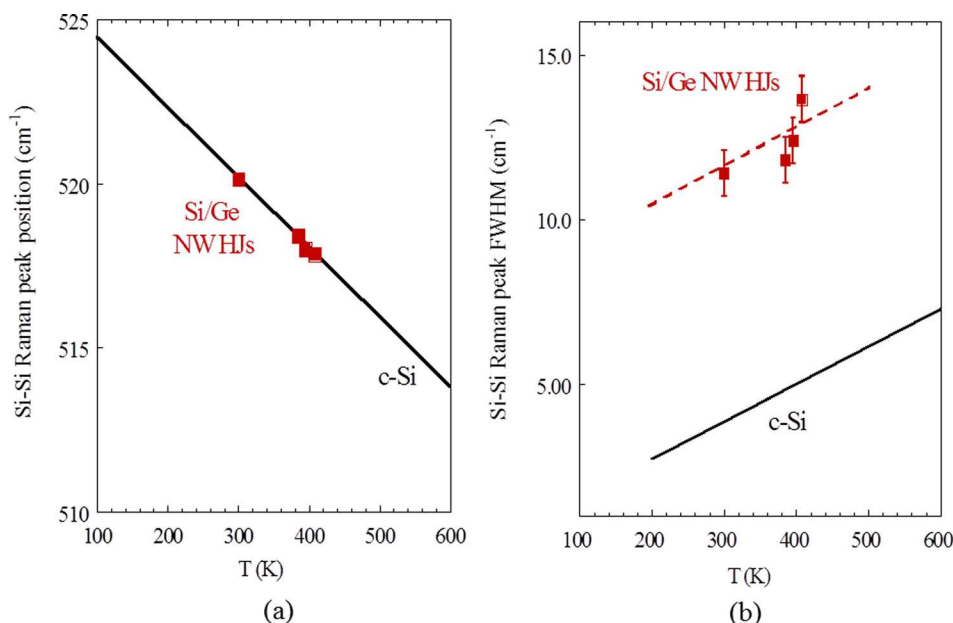


FIG. 10. Measured temperature dependencies of (a) the Si-Si Raman peak position and (b) the Si-Si Raman peak FWHM in Si/Ge NW HJs (squares) compared with that of c-Si (solid lines).

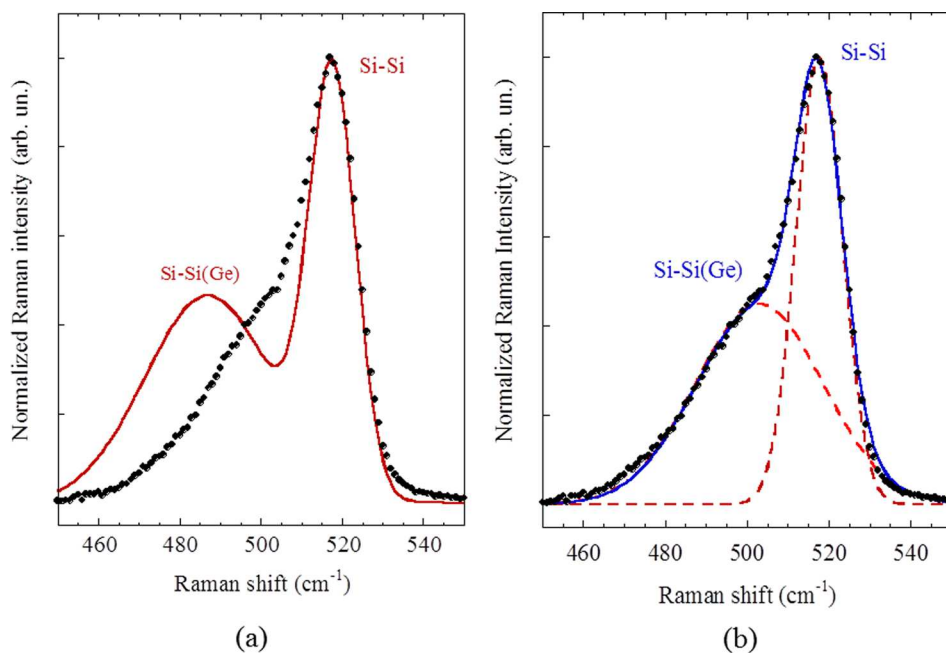


FIG. 11. (a) Comparison of the calculated (solid line) and measured (points) Raman spectrum of Si/Ge NW HJs under an excitation intensity of  $700 \text{ W/cm}^2$ . (b) The curve-resolved (dashed lines) experimental Raman spectrum of Si/Ge NW HJs. Raman peaks associated with Si-Si and Si-Si(Ge) vibrations are marked.

to reduce the sample thermal conductivity. Also, the reduced ratio of Si-Si to Si-Si(Ge) Raman peak intensities under higher laser intensity (Fig. 7(c)) is consistent with the assumption that at higher temperature light absorption in Si/Ge NW HJs increases and a smaller number of photons reach the c-Si substrate.

While the Si-Si Raman peak shift toward lower wavenumbers in Si/Ge NW HJs under increasing laser excitation is explained by the sample temperature increase due to absorption of the intense laser radiation, the Si-Si(Ge) Raman peak under the same conditions shifts in the opposite direction (Fig. 7(a)). Figure 11(a) compares the experimental Raman spectrum with the Raman spectrum simulated under the assumption that both Si-Si and Si-Si(Ge) Raman peaks due to the temperature increase should shift toward lower wavenumbers. The discrepancy in the simulated (Fig. 11(a)) and experimentally (Fig. 11(b)) observed positions of the Si-Si(Ge) Raman peak is  $\sim 15 \text{ cm}^{-1}$ , and it can be associated with a considerable laser heating induced thermal stress of the order of 2–3 GPa.<sup>49,50</sup> Stress is known to affect the Raman polarization dependence in Si/SiGe nanostructures,<sup>51</sup> and this notion explains the experimental data shown in Fig. 8. Also, assuming that the PL1 feature is attributed to band-to-band radiative carrier recombination in the Si segment close to the Si/Ge NW HJ, the estimated value of stress (2–3 GPa) is consistent with the compressive stress required to shift the PL1 peak toward higher photon energy by  $\sim 60 \text{ meV}$ . Note that at room temperature the PL measurements were performed using an excitation intensity approaching  $600 \text{ W/cm}^2$ .

Under  $600\text{--}700 \text{ W/cm}^2$  intensity of laser excitation, the sample temperature increase of  $\Delta T \approx 110 \text{ K}$  is quite large. Most of the 458 nm laser radiation is absorbed by the top (Ge) segment of the Si/Ge NW HJs, and heat flow is directed toward the c-Si substrate, which can be considered as a heat sink. The Si and Ge segments of the Si/Ge NW HJs are at least 500 nm long and the SiGe interface alloy layer is only 8 nm thick, but the difference in their thermal conductivity

could be more than 50 times;<sup>48</sup> thus, all segments of the NW (Ge, Si, and SiGe) contribute to the overall thermal conductivity and the observed temperature increase. Using bulk c-Si, c-Ge, and SiGe alloy parameters (e.g., CTE, Young's modulus, etc.), the estimated thermal stress at the Si/Ge heterointerface, due to the mismatch in Si and Ge CTEs, is  $\sim 0.5 \text{ GPa}$ . The discrepancy thus found compared with the number determined above (2–3 GPa) can be explained by assuming that laser induced heating also slightly bends NWs, possibly due to a non-uniform heat flow, and it creates additional stress in the vicinity of the Si/Ge HJ where the large mismatch in thermal expansion takes place.

#### IV. CONCLUSION

In conclusion, we have demonstrated that axial Si/Ge NW HJs with quality core crystallinity can be fabricated using Au-catalyzed VLS growth. Spontaneous intermixing at the Si/Ge heterointerface and lateral expansion of the Ge segment of the nanowire partially relieves the lattice mismatch induced strain. With a Si/Ge NW diameter in the range 70–120 nm, surface-related structural defects and imperfections do not fully control carrier recombination in the Si/Ge NW HJs, and the PL signal associated with band-to-band electron-hole recombination at the Si/Ge NW HJ has been measured and attributed to the SiGe alloy composition revealed by EDX. The PL associated with the Si segment of the Si/Ge NW HJ exhibits a peak shift toward higher photon energy as the temperature increases from 20 K to above room temperature, indicating compressive stress due to the mismatch in Si and Ge CTEs and, possibly, NW bending. Raman scattering measurements performed under laser excitation varying from 100 to  $700 \text{ W/cm}^2$  clearly show that Si/Ge NW temperature can increase by as much as 110 K. This temperature increase produces an unexpected shift of the Raman peak associated with Si-Si(Ge) vibration mode toward higher wavenumbers indicating strong (2–3 GPa)

compressive strain. This conclusion is supported by the Raman polarization dependence in Si/Ge axial NW HJs.

## ACKNOWLEDGMENTS

This work was supported in part by NSF Grant No. ECCS-1027770, Hewlett-Packard Laboratories and the Foundation at NJIT. We thank G. Parent for TEM sample preparation.

- <sup>1</sup>D. Ahn, C. Hong, J. Liu, W. Giziewicz, M. Beals, L. C. Kimerling, J. Michel, J. Chen, and F. X. Kärtner, *Opt. Express* **15**, 3916 (2007).
- <sup>2</sup>J. Michel, J. Liu, and L. C. Kimerling, *Nat. Photonics* **4**, 527 (2010).
- <sup>3</sup>S. Assefa, F. Xia, S. W. Bedell, Y. Zhang, T. Topuria, P. M. Rice, and Y. A. Vlasov, *Opt. Express* **18**, 4986 (2010).
- <sup>4</sup>T. Yin, R. Cohen, M. M. Morse, G. Sarid, Y. Chetrit, D. Rubin, and M. J. Paniccia, *Opt. Express* **15**, 13965 (2007).
- <sup>5</sup>J. Liu, X. Sun, R. Camacho-Aguilera, L. C. Kimerling, and J. Michel, *Opt. Lett.* **35**, 679 (2010).
- <sup>6</sup>R. E. Camacho-Aguilera, Y. Cai, N. Patel, J. T. Bessette, M. Romagnoli, L. C. Kimerling, and J. Michel, *Opt. Express* **20**, 11316 (2012).
- <sup>7</sup>J. Liu, X. Sun, L. C. Kimerling, and J. Michel, *Opt. Lett.* **34**, 1738 (2009).
- <sup>8</sup>D. J. Paul, *Semicond. Sci. Technol.* **19**, R75 (2004).
- <sup>9</sup>Y. Shiraki and A. Sakai, *Surf. Sci. Rep.* **59**, 153 (2005).
- <sup>10</sup>H. Ye and J. Yu, *Sci. Technol. Adv. Mater.* **15**, 024601 (2014).
- <sup>11</sup>K. Saraswat, C. O. Chui, T. Krishnamohan, D. Kim, A. Nayfeh, and A. Pethe, *Mater. Sci. Eng., B* **135**, 242 (2006).
- <sup>12</sup>S. S. Iyer, G. L. Patton, J. Stork, B. S. Meyerson, and D. L. Harnam, *IEEE Trans. Electron Devices* **36**, 2043 (1989).
- <sup>13</sup>D. K. Nayak, K. Goto, A. Yutani, J. Murota, and Y. Shiraki, *IEEE Trans. Electron Devices* **43**, 1709 (1996).
- <sup>14</sup>V. A. Shah, A. Dobbie, M. Myronov, and D. R. Leadley, *J. Appl. Phys.* **107**, 064304 (2010).
- <sup>15</sup>Y. W. Mo, D. E. Savage, B. S. Swartzentruber, and M. G. Lagally, *Phys. Rev. Lett.* **65**, 1020 (1990).
- <sup>16</sup>O. G. Schmidt, O. Kienzle, Y. Hao, K. Eberl, and F. Ernst, *Appl. Phys. Lett.* **74**, 1272 (1999).
- <sup>17</sup>J. M. Baribeau, X. Wu, N. L. Rowell, and D. J. Lockwood, *J. Phys.: Condens. Matter* **18**, R139 (2006).
- <sup>18</sup>H. K. Shin, D. J. Lockwood, and J. M. Baribeau, *Solid State Commun.* **114**, 505 (2000).
- <sup>19</sup>R. S. Wagner, in *Whisker Technology*, edited by A. P. Levitt (Wiley, New York, 1970), p. 47.
- <sup>20</sup>T. I. Kamins, X. Li, R. S. Williams, and X. Liu, *Nano Lett.* **4**, 503 (2004).
- <sup>21</sup>J. B. Hannon, S. Kodambaka, F. M. Ross, and R. M. Tromp, *Nature* **440**, 69 (2006).
- <sup>22</sup>N. D. Zakharov, P. Werner, G. Gerth, L. Schubert, L. Sokolov, and U. Gösele, *J. Cryst. Growth* **290**, 6 (2006).
- <sup>23</sup>L. J. Lauhon, M. S. Gudiksen, D. Wang, and C. M. Lieber, *Nature* **420**, 57 (2002).
- <sup>24</sup>J. Xiang, W. Lu, Y. Hu, Y. Wu, H. Yan, and C. M. Lieber, *Nature* **441**, 489 (2006).
- <sup>25</sup>G. Kästner and U. Gösele, *Philos. Mag.* **84**, 3803 (2004).
- <sup>26</sup>E. Ertekin, P. A. Greaney, D. C. Chrzan, and T. D. Sands, *J. Appl. Phys.* **97**, 114325 (2005).
- <sup>27</sup>H. Y. Chang, L. Tsybeskov, S. Sharma, T. I. Kamins, X. Wu, and D. J. Lockwood, *Appl. Phys. Lett.* **95**, 133120 (2009).
- <sup>28</sup>S. Sharma, T. I. Kamins, and R. S. Williams, *Appl. Phys. A* **80**, 1225 (2005).
- <sup>29</sup>B. V. Kamenev, V. Sharma, L. Tsybeskov, and T. I. Kamins, *Phys. Status Solidi A* **202**, 2753 (2005).
- <sup>30</sup>K. Brunner, *Rep. Prog. Phys.* **65**, 27 (2002).
- <sup>31</sup>B. V. Kamenev, L. Tsybeskov, J. M. Baribeau, and D. J. Lockwood, *Appl. Phys. Lett.* **84**, 1293 (2004).
- <sup>32</sup>L. Tsybeskov, K. L. Moore, D. G. Hall, and P. M. Fauchet, *Phys. Rev. B* **54**, R8361 (1996).
- <sup>33</sup>F. Cerdeira, W. Dreybrodt, and M. Cardona, *Solid State Commun.* **10**, 591 (1972).
- <sup>34</sup>M. I. Alonso and K. Winer, *Phys. Rev. B* **39**, 10056 (1989).
- <sup>35</sup>M. Ben-Ishai and F. Patolsky, *Nano Lett.* **12**, 1121 (2012).
- <sup>36</sup>C. Mouchet, L. Latu-Romain, C. Cayron, E. Rouviere, C. Celle, and J. P. Simonato, *Nanotechnology* **19**, 335603 (2008).
- <sup>37</sup>M. Hanke, C. Eisenschmidt, P. Werner, N. D. Zakharov, F. Syrowatka, F. Heyroth, P. Schäfer, and O. Kononov, *Phys. Rev. B* **75**, 161303(R) (2007).
- <sup>38</sup>R. Dujardin, V. Poydenot, T. Devillers, V. Favre-Nicolin, P. Gentile, and A. Barski, *Appl. Phys. Lett.* **89**, 153129 (2006).
- <sup>39</sup>J. Jie, W. Zhang, K. Peng, G. Yuan, C. S. Lee, and S. T. Lee, *Adv. Funct. Mater.* **18**, 3251 (2008).
- <sup>40</sup>Y. Wang, V. Schmidt, S. Senz, and U. Gösele, *Nat. Nanotechnol.* **1**, 186 (2006).
- <sup>41</sup>S. Sharma, T. I. Kamins, and R. S. Williams, *J. Cryst. Growth* **267**, 613 (2004).
- <sup>42</sup>M. V. Fischetti and S. E. Laux, *J. Appl. Phys.* **80**, 2234 (1996).
- <sup>43</sup>N. Modi, D. J. Lockwood, X. Wu, J.-M. Baribeau, and L. Tsybeskov, *J. Appl. Phys.* **111**, 114313 (2012).
- <sup>44</sup>L. Tsybeskov and D. J. Lockwood, *Proc. IEEE* **97**, 1284 (2009).
- <sup>45</sup>R. R. Reeber and K. Wang, *Mater. Chem. Phys.* **46**, 259 (1996).
- <sup>46</sup>T. R. Hart, R. L. Aggarwal, and B. Lax, *Phys. Rev. B* **1**, 638 (1970).
- <sup>47</sup>J. Menendez and M. Cardona, *Phys. Rev. B* **29**, 2051 (1984).
- <sup>48</sup>H. Y. Chang and L. Tsybeskov, in *Silicon Nanocrystals: Fundamentals, Synthesis and Applications*, edited by L. Pavesi and R. Turan (Wiley-VCH Verlag, 2010), pp. 5105–5154.
- <sup>49</sup>B. A. Weinstein and G. J. Piermarini, *Phys. Rev. B* **12**, 1172 (1975).
- <sup>50</sup>S. H. Wei and A. Zunger, *Phys. Rev. B* **60**, 5404 (1999).
- <sup>51</sup>B. V. Kamenev, H. Grebel, L. Tsybeskov, T. I. Kamins, R. S. Williams, J. M. Baribeau, and D. J. Lockwood, *Appl. Phys. Lett.* **83**, 5035 (2003).